arXiv:2603.09418v1 [cs.CV] 10 Mar 2026

CIGPose: Causal Intervention Graph Neural Network for Whole-Body Pose Estimation

Bohao Li[1] Zhicheng Cao[2*] Huixian Li[1*] Yangming Guo[3*]
[1]School of Computer Science, Northwestern Polytechnical University
[2]Xidian University
[3]School of Cybersecurity, Northwestern Polytechnical University
bh_li@mail.nwpu.edu.cn, zccao@xidian.edu.cn, {lihuixian, yangming_g}@nwpu.edu.cn

Abstract

State-of-the-art whole-body pose estimators often lack robustness, producing anatomically implausible predictions in challenging scenes. We posit this failure stems from spurious correlations learned from visual context, a problem we formalize using a Structural Causal Model (SCM). The SCM identifies visual context as a confounder that creates a non-causal backdoor path, corrupting the model's reasoning. We introduce the Causal Intervention Graph Pose (CIGPose) framework to address this by approximating the true causal effect between visual evidence and pose. The core of CIGPose is a novel Causal Intervention Module: it first identifies confounded keypoint representations via predictive uncertainty and then replaces them with learned, context-invariant canonical embeddings. These deconfounded embeddings are processed by a hierarchical graph neural network that reasons over the human skeleton at both local and global semantic levels to enforce anatomical plausibility. Extensive experiments show CIGPose achieves a new state-of-the-art on COCO-WholeBody. Notably, our CIGPose-x model achieves 67.0% AP, surpassing prior methods that rely on extra training data. With the additional UBody dataset, CIGPose-x is further boosted to 67.5% AP, demonstrating superior robustness and data efficiency. The codes and models are publicly available at https://github.com/53mins/CIGPose.

1. Introduction

Whole-body pose estimation—localizing dense anatomical keypoints [3, 11, 18] for the entire human body, including the limbs, face, and hands—is fundamental for applications like 3D mesh recovery [24, 26, 45], motion generation [25, 56], and human-robot interaction [7, 39]. Despite deep learning's progress, state-of-the-art models [15, 16, 55] lack robustness, often failing in real-world scenarios with heavy occlusion, clutter, or difficult lighting. This fragility suggests high-capacity models [19, 52] rely on superficial statistics rather than anatomical understanding.

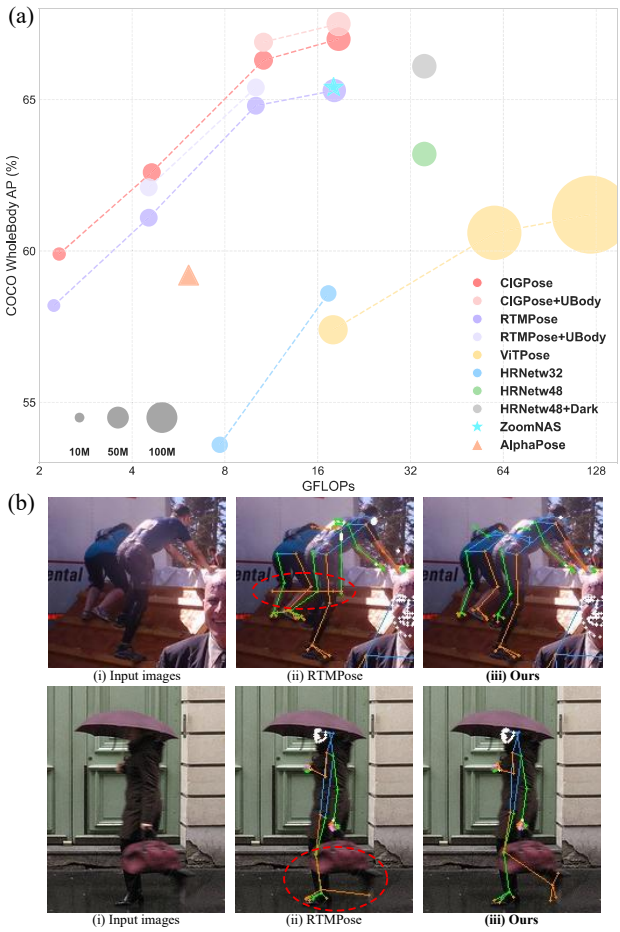

Figure 1. (a) Comparison of CIGPose with related models for whole-body pose estimation on COCO-WholeBody. (b) Qualitative comparison between CIGPose-x and RTMPose-x [15].

*Corresponding authors.

We posit the root cause is visual confounding [29], leading to failures like misidentifying background patterns as limbs, as shown in Fig. 1(b). These errors stem from spurious correlations; for example, a network might associate a "backrest" with a "torso" due to co-occurrence in training data. This context C confounds the extracted features F and the final pose Y, creating a non-causal backdoor path $F \leftarrow X \leftarrow C \rightarrow Y$ that corrupts the model's prediction, which is based on the observational distribution $P(Y|F)$. True robustness requires learning the interventional distribution $P(Y|do(F))$, using the do-operator [35] to remove the confounder's influence.

We introduce the **C**ausal **I**ntervention **G**raph Neural Network for Whole-body Pose Estimation (CIGPose), a framework approximating the causal intervention $P(Y|do(F))$. Our core contribution is a Causal Intervention Module (CIM) that identifies confounded keypoint embeddings using predictive uncertainty as a proxy. The CIM then replaces these corrupted embeddings with learned, context-invariant canonical embeddings, blocking the backdoor path and forcing the model to use causally sound evidence.

A hierarchical graph neural network then processes these deconfounded embeddings to enforce global anatomical plausibility. The GNN models the human skeleton at multiple semantic levels, first local kinematics, then long-range dependencies, enforcing structural consistency on a causal foundation to produce accurate and anatomically coherent poses.

CIGPose establishes a new state-of-the-art on COCO-WholeBody [18], as shown in Fig. 1(a), and its effectiveness is also assessed on COCO [27] and CrowdPose [23] datasets. Trained only on COCO-WholeBody [18], our CIGPose-x model reaches 67.0% AP, outperforming competitors that use additional datasets. When trained with the additional UBody [26] dataset, its performance rises to 67.5% AP, surpassing 66.5% AP of DWPose-l [55] and demonstrating superior robustness and data efficiency.

In summary, our main contributions are:

- We formalize 2D whole-body pose estimation within a causal framework, identifying visual context as a critical confounder that creates spurious correlations.
- We propose a novel Causal Intervention Module (CIM) that approximates a causal do-operation by identifying and replacing confounded keypoint embeddings with learned canonical representations.
- We introduce a hierarchical graph neural network that explicitly models anatomical structure on deconfounded embeddings, enhancing global pose consistency.
- CIGPose achieves state-of-the-art performance on multiple large-scale benchmarks, demonstrating superior accuracy and robustness in complex scenes.

2. Related Work

2.1. 2D Whole-body Pose Estimation

Modern top-down 2D pose estimation [18, 50] evolved from high-resolution CNNs [42] to Vision Transformers [51, 52, 58], with a concurrent focus on efficiency [15, 55]. Yet, SOTA estimators fail in complex scenes due to spurious correlations learned from visual context. Prior work improved robustness via knowledge distillation [55] or massive datasets [16, 19] but did not address confounding directly. Our causal framework achieves inherent robustness by identifying and mitigating visual confounders, improving both accuracy and data efficiency. Other works address specific robustness challenges. ProbPose [37] for out-of-image keypoints and robustness for 2D-to-3D lifters [12]. Video-based whole-body motion estimation also explores robustness, such as REWIND [21].

2.2. Graph Neural Networks for Human Pose Estimation

The skeleton's structure is a natural fit for GNNs, used to enforce anatomical constraints by modeling joint kinematics [13, 36, 40, 63]. Hierarchical GNNs [20, 22, 38, 60, 64], inspired by action recognition, refine poses by reasoning at multiple semantic levels, from local limbs to global inter-part relations. Yet, these methods [1, 43, 44, 62] are vulnerable to confounded inputs; a GNN will propagate errors from corrupted initial keypoint representations [17]. Many are also designed for video [10, 54, 57, 60], integrating temporal information, unlike our single-image task. Our framework is to address this issue of error propagation. A causal intervention module precedes the GNN, ensuring structural reasoning occurs on a deconfounded embedding set, making the model more robust.

2.3. Causal Inference

Causal inference [34] improves robustness by learning the interventional distribution $P(Y|do(X))$ instead of the observational $P(Y|X)$. In computer vision, scene context is a known confounder creating a backdoor path, formalized with Structural Causal Models (SCMs) [33] in tasks like semantic segmentation [61] and VQA [32]. The backdoor adjustment formula is intractable in high-dimensional vision, leading to practical approximations [14, 41, 59] like marginalizing out the context. Our work introduces a novel mechanism: we identify confounded embeddings via predictive uncertainty and replace them with learned, context-invariant canonical embeddings. This counterfactual replacement severs the backdoor path, offering a new approach to causal learning in vision. Causal learning has also been recently applied to object pose estimation. Notably, CleanPose [28] addresses data biases by integrating causal learning with knowledge distillation. While their work also

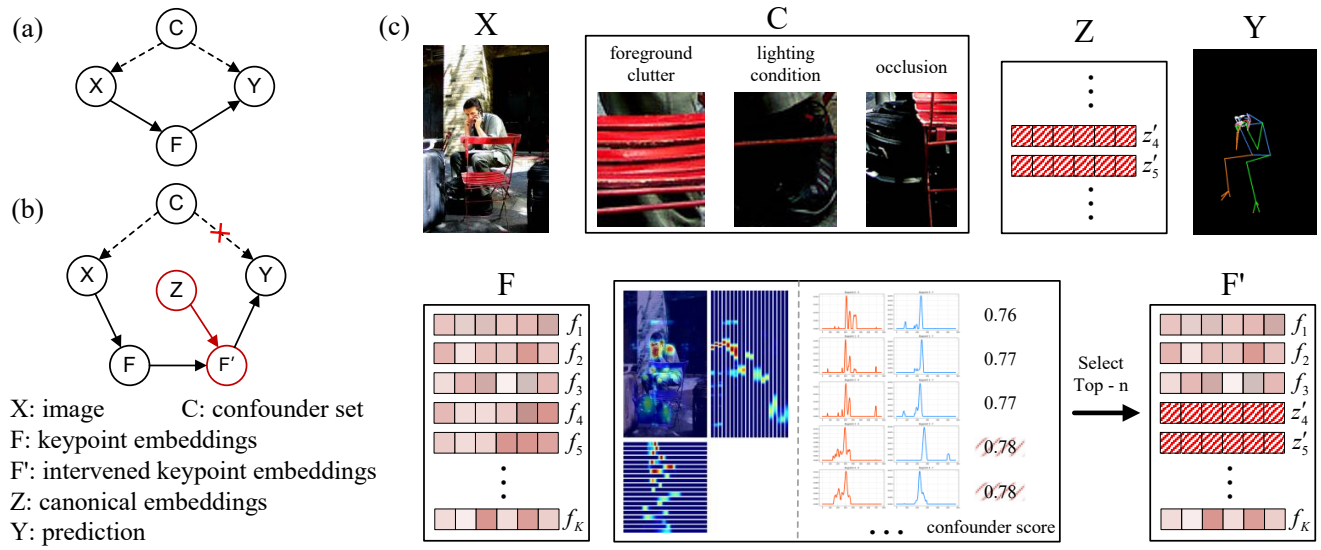

Figure 2. (a) The proposed Structural Causal Model (SCM) for keypoint estimation, (b) The intervened SCM after applying the *do*-operator to the keypoint embeddings, (c) The realization of each component within our Causal Intervention Module (CIM).

mitigates spurious correlations, it employs a front-door adjustment, distinct from our intervention strategy.

3. Method

3.1. Structural Causal Model and Theoretical Goal

We formalize pose estimation using the Structural Causal Model (SCM) [33] in Fig. 2(a), defining relationships between the image X, unobserved confounders C, keypoint embeddings F, and prediction Y.

- $C \rightarrow X$: Confounder set C, such as specific lighting conditions or foreground clutter, is inherent to the captured scene and thus causally determines the visual content of the input image X.
- $X \rightarrow F$: A keypoint encoder processes the input image X to produce a set of initial keypoint embeddings F.
- $C \rightarrow Y$: This path shows the core confounding problem: The model learns a spurious, non-causal correlation from the training data between visual context C (*e.g.* "backrest") and true pose Y (*e.g.* a "torso" in a sitting position), thus mistaking context for evidence.
- $F \rightarrow Y$: The prediction head decodes the keypoint embeddings F to produce the final coordinate predictions Y. This represents the true, desired causal path.

The critical issue is the non-causal backdoor path $F \leftarrow X \leftarrow C \rightarrow Y$. This path allows the model to exploit spurious correlations: the feature embeddings F (which are caused by X, which is caused by C) become associated with Y, not through the desired causal path $F \rightarrow Y$, but via the confounding arc $C \rightarrow Y$. A model trained on this confounded data learns the observational distribution $P(Y|F)$, not the true causal relationship.

To eliminate this confounding effect, our goal is to estimate the interventional distribution $P(Y|do(F))$. The *do*-operator [35] signifies this intervention. The intervention aims to block the non-causal backdoor path $F \leftarrow X \leftarrow C \rightarrow Y$. As shown in Fig. 2(b), this is conceptually equivalent to severing the confounding link $C \rightarrow Y$, forcing the model to rely only on the causal path $F \rightarrow Y$. Theoretically, this causal effect can be computed using the backdoor adjustment formula:

$$P(Y|do(F)) = \sum_{c} P(Y|F, c)P(c) \tag{1}$$

However, this formula is intractable in our scenario. The confounder C represents all possible high-dimensional visual contexts and is unobserved, making the summation over c impossible to compute. Therefore, we propose the **C**ausal **I**ntervention **M**odule (CIM), a novel and practical framework designed to approximate this causal intervention. We provide a formal derivation for Eq. (1) using Pearl's *do*-calculus [35] and a theoretical justification for our counterfactual approximation in Appendix A.

3.2. Causal Intervention via Counterfactual Replacement

Our CIM approximates Eq. (1) by identifying confounded embeddings $F_{conf} \subset F$ and replacing them with a "clean", context-invariant representation.

Justification for Counterfactual Replacement. We propose to replace a confounded embedding $f_k \in F_{conf}$ with a learned canonical embedding z_k. These are drawn from a learnable embedding table $Z \in \mathbb{R}^{K \times d_{emb}}$, optimized end-to-end to represent a context-invariant ideal for each

keypoint type. The key insight is that Z, as a set of learnable model parameters, is by construction independent of the specific confounder instance C affecting any given input image, such that $Z \perp C$. By performing this counterfactual intervention $do(f_k := z_k)$, we replace the confounded embedding with an embedding that is independent of C. This action breaks the dependency chain $F \leftarrow X \leftarrow C$, thereby blocking the non-causal backdoor path $F \leftarrow X \leftarrow C \rightarrow Y$.

Justification for Confounder Identification. To intervene selectively, we must identify F_{conf}. We posit that predictive uncertainty is an effective proxy for confounding. The confounder set C creates a conflict between visual evidence F and biased priors (from $C \rightarrow Y$), manifesting as high epistemic uncertainty. While this hypothesis applies generally, validating it against ambiguous, hard-to-label factors like clutter or contextual confusion is intractable. However, we can robustly validate our proxy against heavy occlusion, which is arguably the most severe and clearly-defined class of confounder in pose estimation.

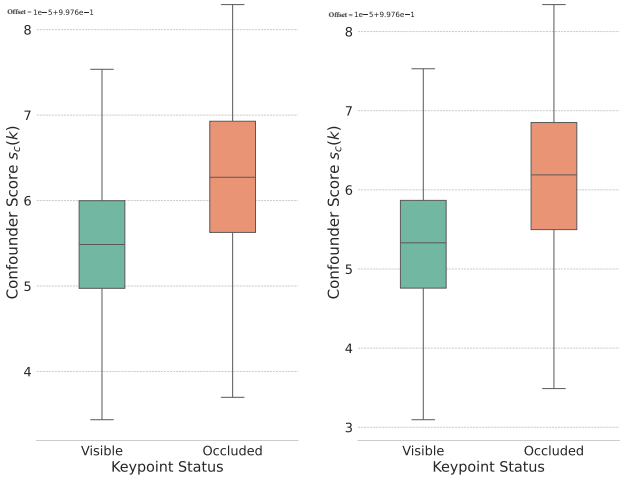

(a) Limb Keypoints (b) All Keypoints

Figure 3. Validation of confounder score $s_c(k)$ on COCO-WholeBody [18]. The confounder score is significantly higher for occluded keypoints than for visible ones, for both (a) easily occluded limb keypoints and (b) all keypoints combined.

High uncertainty is reflected in diffuse posterior probability distributions (see Appendix B). We quantitatively validate this in Fig. 3. This figure plots our proposed confounder score $s_c(k)$ (defined in Eq. (2)) against the keypoint's ground-truth occlusion status on the COCO-WholeBody [18] validation set. As shown in Fig. 3(a) and Fig. 3(b), occluded keypoints exhibit a significantly higher median and wider distribution of confounder scores compared to visible keypoints. This positive correlation supports our assumption that predictive uncertainty is a reliable proxy for detecting this critical type of confounding. We hypothesize this sensitivity to occlusion-induced ambiguity also grants robustness to other non-occlusion-based confounders, supported by our model's performance in complex scenes as shown in Fig. 6. Further details on the network architecture of CIM are available in Appendix C.

Implementation Details. Based on this justification, the CIM (illustrated in Fig. 2(c)) operates via a two-step process:

Step 1. Confounder Identification. Given the initial keypoint embeddings F, we first generate 1D coordinate heatmaps, normalized into posterior probability distributions $(P_{k,x}, P_{k,y})$. We use the concentration of this distribution to quantify predictive ambiguity. A low peak signals high uncertainty, which we use as a proxy for confounding. We define the confounder score for each keypoint as:

$$s_c(k) = 1 - \frac{1}{2}(\max(P_{k,x}) + \max(P_{k,y})) \tag{2}$$

The keypoints with the top-n highest scores $s_c(k)$ are selected for intervention.

Step 2. Counterfactual Embedding Replacement. For each selected embedding $f_k \in F$, we perform the intervention $do(f_k := z_k)$ by replacing it with its corresponding canonical embedding z_k from the learnable table Z. This substitution creates the deconfounded, or "cleaned", embedding set F':

$$f'_k = \begin{cases} z_k, & \text{if } k \text{ is selected for intervention} \\ f_k, & \text{otherwise} \end{cases} \tag{3}$$

The final prediction Y is then derived from this cleaned set F'. By replacing confounded embeddings with their ideal counterparts, we block the spurious causal path from C and force the model to reason from a more robust, causally sound representation.

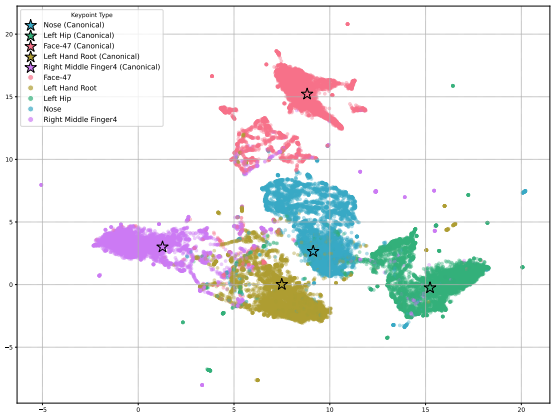

Figure 4. UMAP visualization of initial contextual embeddings vs. their corresponding learned canonical embeddings.

Analysis of Canonical Embeddings. To validate our assumption that Z learns context-invariant ideals, we visual-

ize the embeddings using UMAP in Fig. 4. The initial contextual embeddings F (from the encoder) for a single keypoint type form a diffuse cluster, reflecting variance from visual confounders. In contrast, the corresponding learned canonical embedding z_k (from Z) is learned as a single, highly concentrated point. This demonstrates that our model successfully learns a stable, context-invariant representation for each keypoint, which serves as the "causal ideal" during intervention. The clear separation between canonical embeddings for different keypoint types further indicates their semantic distinctiveness.

3.3. Hierarchical Graph Reasoning on Deconfounded Embeddings

To enforce global anatomical constraints on the purified embeddings F', we employ a two-stage hierarchical graph neural network (GNN). Our design, inspired by HD-GCN [20], first models local anatomical regions before reasoning about their global inter-relationships, as shown in Fig. 5.

Intra-Part Relational Modeling. The first stage uses an EdgeConv [47] layer over the standard anatomical skeleton graph $\mathcal{G}_p = (\mathcal{V}, \mathcal{E}_p)$, where edges $\mathcal{E}_p$ represent physical connections. This models local kinematic relationships by updating each keypoint embedding based on its neighbors.

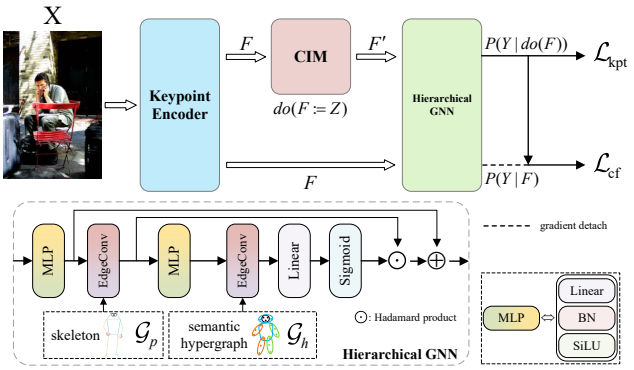

Figure 5. Overview of our CIGPose architecture. During training, embeddings are processed in two paths: (1) a counterfactual path where our CIM module deconfounds them before the Hierarchical GNN, and (2) an observational path using original embeddings for consistency. Inference relies solely on the counterfactual path.

Inter-Part Contextual Attention. The second stage captures long-range dependencies using a semantic hypergraph, denoted as $\mathcal{G}_h$. We predefine hyperedges $\mathcal{E}_h$ as functional keypoint groups (*e.g.*'left hand'). A representation for each hyperedge g_e is computed by aggregating its constituent keypoint embeddings: $g_e = \frac{1}{|e|}\sum_{k\in e} f'_k$. These hyperedge representations then exchange information via message-passing to become context-aware. Finally, these context-aware representations generate channel-wise attention weights to modulate and refine the keypoint embeddings, producing the final, anatomically coherent embeddings F'':

$$f''_k = f'_k \odot \left(\frac{1}{|\mathcal{E}_k|} \sum_{e\in\mathcal{E}_k} \sigma(\psi_a(g'_e)) \right) \tag{4}$$

where g'_e is the updated, context-aware representation for a hyperedge e, ψ_a is an MLP, σ is the sigmoid function, and $\mathcal{E}_k$ is the set of hyperedges containing keypoint k. This hierarchical process produces embeddings that are both deconfounded and anatomically plausible. We provide expanded implementation details for the hierarchical GNN components in Appendix C.

3.4. Joint Optimization with Counterfactual Consistency

CIGPose is trained end-to-end with a composite objective that combines a primary supervised loss with a regularizer to ensure our causal interventions are meaningful (see Fig. 5).

The primary prediction loss, $\mathcal{L}_{\text{kpt}}$, is applied to the final output of the counterfactual path. It minimizes the KL divergence between the final predicted pose distribution $P(Y|do(F))$ and the ground-truth distribution Q:

$$\mathcal{L}_{\text{kpt}} = \sum_{k=1}^{K} w_k \cdot D_{KL}(Q_k \,||\, P(Y_k|do(F))) \tag{5}$$

where w_k weights keypoints by their ground-truth visibility.

To ensure interventions are targeted and canonical embeddings Z are meaningful, we introduce a Counterfactual Consistency Loss, $\mathcal{L}_{\text{cf}}$. It regularizes the model by penalizing the divergence between the prediction from the observational path, $P(Y|F)$, and the prediction from the counterfactual path, $P(Y|do(F))$. This loss is only applied to the set of stable keypoints S, which is defined as the $K-n$ keypoints with the lowest confounder scores $s_c(k)$ that were not selected for intervention in Eq. (3).

$$\mathcal{L}_{\text{cf}} = \frac{1}{|S|} \sum_{k\in S} D_{KL}(\text{sg}[P(Y_k|F)]) \,||\, P(Y_k|do(F)) \tag{6}$$

where the stop-gradient operator, sg$[\cdot]$, treats the observational prediction as a fixed target. This encourages the intervention to only alter confounded representations without disrupting reliable ones. The final training objective is a weighted sum of these two components: $\mathcal{L} = \mathcal{L}_{\text{kpt}} + \lambda\mathcal{L}_{\text{cf}}$, where λ is a weight hyperparameter.

4. Experiments

4.1. Datasets and Evaluation Metrics

Datasets. We conduct extensive experiments on four challenging benchmarks to validate our method. COCO [27] is

Table 1. Whole-body pose estimation results on COCO-WholeBody [18, 50] V1.0 dataset. "*" denotes the model that relies on two-stage distillation and additional training data from the UBody dataset [26]. "†" indicates multi-scale testing. Flip test is used.

	Method	Input Size	GFLOPs	whole-body		body		foot		face		hand	
				AP	AR	AP	AR	AP	AR	AP	AR	AP	AR
Whole-body	SN† [11]	N/A	272.3	32.7	45.6	42.7	58.3	9.9	36.9	64.9	69.7	40.8	58.0
	OpenPose [3]	N/A	451.1	44.2	52.3	56.3	61.2	53.2	64.5	76.5	84.0	38.6	43.3
Bottom-up	PAF† [2]	512×512	329.1	29.5	40.5	38.1	52.6	5.3	27.8	65.6	70.1	35.9	52.8
	AE [31]	512×512	212.4	44.0	54.5	58.0	66.1	57.7	72.5	58.8	65.4	48.1	57.4
Top-down	SimpleBaseline [49]	384×288	20.4	57.3	67.1	66.6	74.7	63.5	76.3	73.2	81.2	53.7	64.7
	HRNet [42]	384×288	16.0	58.6	67.4	70.1	77.3	58.6	69.2	72.7	78.3	51.6	60.4
	PVT [46]	384×288	19.7	58.9	68.9	67.3	76.1	66.0	79.4	74.5	82.2	54.5	65.4
	FastPose50-dcn-si [8]	256×192	6.1	59.2	66.5	70.6	75.6	70.2	77.5	77.5	82.5	45.7	53.9
	ZoomNet [18]	384×288	28.5	63.0	74.2	74.5	81.0	60.9	70.8	88.0	92.4	57.9	73.4
	ZoomNAS [50]	384×288	18.0	65.4	74.4	74.0	80.7	61.7	71.8	88.9	93.0	62.5	74.0
	ViTPose+-H [52]	256×192	122.9	61.2	-	75.9	-	77.9	-	63.3	-	54.7	-
	RTMPose-m [15]	256×192	2.2	58.2	67.4	67.3	75.0	61.5	75.2	81.3	87.1	47.5	58.9
	RTMPose-l [15]	256×192	4.5	61.1	70.0	69.5	76.9	65.8	78.5	83.3	88.7	51.9	62.8
	RTMPose-l [15]	384×288	10.1	64.8	73.0	71.2	78.1	69.3	81.1	88.2	91.9	57.9	67.7
	RTMPose-x [15]	384×288	18.1	65.3	73.3	71.4	78.4	69.2	81.0	88.9	92.3	59.0	68.5
	RTMPose-l + UBody	256×192	4.5	62.1	70.6	69.7	76.9	65.5	78.1	84.1	89.3	55.1	65.4
	RTMPose-l + UBody	384×288	10.1	65.4	73.2	71.0	77.9	68.6	80.2	88.5	92.2	60.6	69.9
	DWPose-m* [55]	256×192	2.2	60.6	69.5	68.5	76.1	63.6	77.2	82.8	88.1	52.7	63.4
	DWPose-l* [55]	256×192	4.5	63.1	71.7	70.4	77.7	66.2	79.0	84.3	89.4	56.6	66.5
	DWPose-l* [55]	384×288	10.1	66.5	74.3	72.2	78.9	70.4	81.7	88.7	92.1	62.1	71.0
	CIGPose-m	256×192	2.3	59.9	69.4	69.0	76.6	64.3	77.6	82.1	88.3	49.7	61.6
	CIGPose-l	256×192	4.6	62.6	71.9	71.2	78.5	69.0	80.8	83.3	89.1	54.0	64.9
	CIGPose-l	384×288	10.7	66.3	74.9	73.0	79.9	72.0	83.3	88.3	92.3	59.8	70.0
	CIGPose-x	384×288	18.7	67.0	75.4	73.5	80.3	72.3	83.5	88.1	92.4	60.2	71.0
	CIGPose-l + UBody	384×288	10.7	66.9	75.1	73.1	79.6	72.3	82.7	88.0	92.5	61.2	71.6
	CIGPose-x + UBody	384×288	18.7	67.5	75.5	73.5	80.1	70.3	81.6	88.4	92.7	62.6	72.6

a standard benchmark for 2D human pose estimation, for which we use the train2017 set for training and val2017 set for evaluation. COCO-WholeBody [18] extends COCO with dense annotations of 133 keypoints, enabling comprehensive whole-body analysis. UBody [26] is a large-scale dataset featuring over 1M frames from 15 real-world scenarios. Following DWPose [55], we sub-sample the videos at an interval of 10 frames for both training and validation. This dataset is used in conjunction with COCO-WholeBody to assess the generalization capability of our model. Finally, CrowdPose [23] is utilized to evaluate model performance in highly crowded and occluded scenes. We follow the standard protocol [23] of training on its trainval set and evaluating on the test set.

Evaluation Metrics. We follow the standard evaluation protocols for each dataset. For COCO [27] and COCO-WholeBody [18], we report the standard OKS-based Average Precision (AP) and Average Recall (AR). For CrowdPose [23], we report AP, AP_{easy}, AP_{medium}, and AP_{hard} as defined in [23].

4.2. Implementation Details

We implement CIGPose in the MMPose toolbox [5], employing RTMPose [15] as the keypoint encoder with 256×192 and 384×288 inputs. To ensure a fair and reproducible comparison, all models are initialized with public RTMPose weights, which were pre-trained on COCO [27] and AIC [48] datasets. We train for up to 420 epochs using the AdamW optimizer (weight decay 0.05) and a cosine annealing learning rate schedule with a 1000-iteration linear warm-up. Our data augmentation follows RTMPose, including its two-stage fine-tuning approach. The weight λ of counterfactual consistency loss $\mathcal{L}_{\text{cf}}$ is fixed at 0.1. During evaluation, we apply flip test and use person detection

boxes consistent with RTMPose [15], except for UBody [26] where ground-truth boxes are used. Training is conducted on a single NVIDIA GeForce RTX 5090 for COCO [27] and CrowdPose [23] and 8 NVIDIA GeForce RTX 4090 GPUs for COCO-WholeBody [18] and UBody [26]. We provide an expanded description of our network architecture and training settings in Appendix C, and our full two-stage data augmentation strategy in Appendix D.

4.3. Comparison with State-of-the-art Methods

We evaluate our proposed CIGPose framework against state-of-the-art methods on three challenging public benchmarks: COCO-WholeBody [18], COCO [27], and CrowdPose [23].

COCO-WholeBody. As shown in Tab. 1, CIGPose establishes a new SOTA on the COCO-WholeBody [18] dataset. Trained solely on COCO-WholeBody, our CIGPose-x achieves 67.0% AP, surpassing DWPose-l [55] (66.5% AP), which relies on two-stage distillation and additional data from UBody [26]. This highlights our framework's superior data efficiency and robustness. With the UBody dataset, CIGPose-x's performance further improves to 67.5% AP. Notably, our CIGPose-l (384×288) reaches 66.3% AP, outperforming the larger RTMPose-x [15] (65.3% AP) with fewer GFLOPs. Qualitative results in Fig. 6 confirm our model's ability to produce more anatomically plausible poses in challenging scenes.

Table 2. Comparisons of CIGPose and SOTA methods on COCO val set [27]. The default input resolution is 256×192, "†" denotes the input resolution is 384×288.

Method	#Params	GFLOPs	COCO Val	
			AP	AR
SimpleBaseline [49]	60M	15.7	73.5	79.0
HRNet† [42]	64M	32.9	76.3	81.2
HRFormer-B† [58]	43M	26.8	77.2	82.0
ViTPose++-B [52]	86M	17.1	77.0	82.6
RTMPose-m [15]	14M	1.9	75.8	80.6
RTMPose-l [15]	28M	4.2	76.5	81.3
RTMPose-l† [15]	28M	9.3	77.3	81.9
CIGPose-m	14M	1.9	76.6	79.3
CIGPose-l	28M	4.2	77.6	80.3
CIGPose-l†	29M	9.4	78.5	81.1

COCO. To demonstrate general applicability, we test on the COCO val2017 benchmark [27] for 17-keypoint pose estimation. CIGPose consistently improves upon its baseline (Tab. 2). For instance, CIGPose-l with a 384×288 input achieves 78.5% AP, a 1.2 AP improvement over the strong RTMPose-l baseline with only a marginal increase in computational cost. This shows our causal mechanisms are beneficial for general pose estimation tasks.

Table 3. Comparisons with SOTA methods on the CrowdPose [23] dataset. The default input resolution is 256×192, "†" denotes the input resolution is 384×288.

Method	#Params	AP	AP_E	AP_M	AP_H
Bottom-up methods					
OpenPose [3]	-	-	62.7	48.7	32.3
HrHRNet [4]	63.8M	65.9	73.3	66.5	57.9
DEKR [9]	65.7M	67.3	74.6	68.1	58.7
SWAHR [30]	63.8M	71.6	78.9	72.4	**63.0**
Top-down methods					
SimpleBaseline [49]	34.0M	60.8	71.4	61.2	51.2
HRNet [42]	28.5M	71.3	80.5	71.4	62.5
TransPose-H [53]	-	71.8	79.5	72.9	62.2
HRFormer-B [58]	43.2M	72.4	80.0	73.5	62.4
RTMPose-m [15]	13.5M	70.6	79.9	71.9	58.2
CIGPose-m	14.4M	71.4	81.0	72.7	58.9
CIGPose-l	28.4M	**73.7**	**82.8**	**75.1**	61.2
CIGPose-l†	28.8M	74.2	82.9	75.6	62.5
CIGPose-x†	50.4M	75.8	84.2	77.3	63.6

CrowdPose. We assess robustness in crowded and occluded scenarios using the CrowdPose [23] dataset. Tab. 3 shows CIGPose achieves competitive results. Specifically, CIGPose-l obtains 73.7% AP, outperforming prior SOTA methods like HRFormer-B [58] (72.4% AP). A larger model, CIGPose-x†, further improves performance to 75.8% AP. The consistent improvements on the medium and hard subsets underscore our method's efficacy in mitigating interference from common confounders like occlusions and cluttered backgrounds.

4.4. Ablation Studies

Table 4. Ablation study of CIGPose on COCO-WholeBody. Values in parentheses are AP/AR gains.

CIM	$\mathcal{G}_h$	$\mathcal{G}_p$	Model	AP	AR
✓	✓	✓	CIGPose-l	66.3 (+1.5)	74.9 (+1.9)
			CIGPose-x	67.0 (+1.7)	75.4 (+2.1)
✗	✓	✓	CIGPose-l	66.0 (+1.2)	74.8 (+1.8)
			CIGPose-x	66.8 (+1.5)	75.5 (+2.2)
✗	✗	✓	CIGPose-l	65.6 (+0.8)	74.6 (+1.6)
			CIGPose-x	66.3 (+1.0)	75.0 (+1.7)
✓	✗	✗	CIGPose-l	65.7 (+0.9)	74.3 (+1.3)
			CIGPose-x	66.1 (+0.8)	74.9 (+1.6)
✗	✗	✗	Baseline [15]	64.8	73.0
				65.3	73.3

Figure 6. Qualitative comparison of CIGPose-x against the baseline RTMPose-x [15] on challenging images. From left to right: input image, RTMPose-x, and CIGPose-x.

We conduct ablation studies on the COCO-WholeBody [18] dataset to dissect the contributions of key components in CIGPose. All models use RTMPose [15] as keypoint encoder and a 384×288 input size.

Effectiveness of Proposed Components. As shown in Tab. 4, we analyze the individual contributions of the Causal Intervention Module (CIM) and the hierarchical GNN components ($\mathcal{G}_p$ and $\mathcal{G}_h$) against the baseline [15]. Adding the hierarchical GNN components ($\mathcal{G}_p$ and $\mathcal{G}_h$) without intervention yields 66.8 AP, demonstrating the value of structural reasoning (+1.5 AP). Introducing our CIM on top of the full GNN further lifts performance to 67.0 AP, a +0.2 AP gain from deconfounding. The full CIGPose-x model achieves a total gain of 1.7 AP over the baseline, highlighting the synergistic effect of performing hierarchical reasoning on deconfounded embeddings. We provide further ablation studies on intervention frequency, the consistency loss weight λ, and alternative intervention strategies in Appendix E.

5. Conclusion

We introduced CIGPose, a novel framework that applies causal intervention to whole-body pose estimation. We proposed using predictive uncertainty as a proxy for confounding and quantitatively validated its effectiveness in identifying heavy occlusion, a critical and severe class of confounders. By replacing these keypoints with learned canonical embeddings, our method mitigates spurious correlations and achieves state-of-the-art results on major 2D benchmarks. Future work will focus on extending our causal framework to more challenging domains, such as 3D and out-of-distribution scenarios. We provide a discussion of the current limitations of our approach, including the potential risks of our intervention strategy and the constraints of our confounding proxy, in Appendix F. This approach opens a promising direction for building more reliable and generalizable pose estimators.

Acknowledgement. This work was supported by the Key Research and Development Program of Shaanxi (2024GXYBXM-543), the Fundamental Research Funds for the Central Universities (QTZX25114), Zhejiang Provincial Excellent Funding for Postdoctoral Researchers (ZJ2025156) and China Postdoctoral Science Foundation (2025M784428).

References

[1] Niloofar Azizi, Mohsen Fayyaz, and Horst Bischof. Occlusion handling in 3d human pose estimation with perturbed positional encoding. In *European Conference on Computer Vision*, pages 441–458. Springer, 2024. 2

[2] Zhe Cao, Tomas Simon, Shih-En Wei, and Yaser Sheikh. Realtime multi-person 2d pose estimation using part affinity fields. In *Proceedings of the IEEE/CVF Conference on Computer Vision and Pattern Recognition*, pages 7291–7299, 2017. 6

[3] Zhe Cao, Gines Hidalgo, Tomas Simon, Shih-En Wei, and Yaser Sheikh. Openpose: Realtime multi-person 2d pose estimation using part affinity fields. *IEEE Transactions on Pattern Analysis and Machine Intelligence*, 43(1):172–186, 2021. 1, 6, 7

[4] Bowen Cheng, Bin Xiao, Jingdong Wang, Honghui Shi, Thomas S Huang, and Lei Zhang. Higherhrnet: Scale-aware representation learning for bottom-up human pose estimation. In *Proceedings of the IEEE/CVF Conference on Computer Vision and Pattern Recognition*, pages 5386–5395, 2020. 7

[5] MMPose Contributors. Openmmlab pose estimation toolbox and benchmark. https://github.com/open-mmlab/mmpose, 2020. 6

[6] Songcheng Du, Yang Zou, Zixu Wang, Xingyuan Li, Ying Li, Changjing Shang, and Qiang Shen. Unsupervised hyperspectral image super-resolution via self-supervised modality decoupling. *International Journal of Computer Vision*, 2026.

[7] Zicong Fan, Omid Taheri, Dimitrios Tzionas, Muhammed Kocabas, Manuel Kaufmann, Michael J Black, and Otmar Hilliges. Arctic: A dataset for dexterous bimanual hand-object manipulation. In *Proceedings of the IEEE/CVF Conference on Computer Vision and Pattern Recognition*, pages 12943–12954, 2023. 1

[8] Hao-Shu Fang, Jiefeng Li, Hongyang Tang, Chao Xu, Haoyi Zhu, Yuliang Xiu, Yong-Lu Li, and Cewu Lu. Alphapose: Whole-body regional multi-person pose estimation and tracking in real-time. *IEEE Transactions on Pattern Analysis and Machine Intelligence*, 45(6):7157–7173, 2023. 6

[9] Zigang Geng, Ke Sun, Bin Xiao, Zhaoxiang Zhang, and Jingdong Wang. Bottom-up human pose estimation via disentangled keypoint regression. In *Proceedings of the IEEE/CVF Conference on Computer Vision and Pattern Recognition*, pages 14676–14686, 2021. 7

[10] Jijie He and Wenwu Yang. Video-based human pose regression via decoupled space-time aggregation. In *Proceedings of the IEEE/CVF Conference on Computer Vision and Pattern Recognition*, pages 1022–1031, 2024. 2

[11] Gines Hidalgo, Yaadhav Raaj, Haroon Idrees, Donglai Xiang, Hanbyul Joo, Tomas Simon, and Yaser Sheikh. Single-network whole-body pose estimation. In *Proceedings of the IEEE/CVF International Conference on Computer Vision*, pages 6982–6991, 2019. 1, 6

[12] Trung-Hieu Hoang, Mona Zehni, Huy Phan, Duc Minh Vo, and Minh N. Do. Improving the robustness of 3d human pose estimation: A benchmark and learning from noisy input. In *Proceedings of the IEEE/CVF Conference on Computer Vision and Pattern Recognition (CVPR) Workshops*, pages 113–123, 2024. 2

[13] Wenbo Hu, Changgong Zhang, Fangneng Zhan, Lei Zhang, and Tien-Tsin Wong. Conditional directed graph convolution for 3d human pose estimation. In *Proceedings of the 29th ACM international conference on multimedia*, pages 602–611, 2021. 2

[14] Daniel Israel, Aditya Grover, and Guy Van den Broeck. High dimensional causal inference with variational backdoor adjustment. *arXiv preprint arXiv:2310.06100*, 2023. 2

[15] Tao Jiang, Peng Lu, Li Zhang, Ningsheng Ma, Rui Han, Chengqi Lyu, Yining Li, and Kai Chen. Rtmpose: Real-time multi-person pose estimation based on mmpose. *arXiv preprint arXiv:2303.07399*, 2023. 1, 2, 6, 7, 8, 3

[16] Tao Jiang, Xinchen Xie, and Yining Li. Rtmw: Real-time multi-person 2d and 3d whole-body pose estimation. *arXiv preprint arXiv:2407.08634*, 2024. 1, 2

[17] Sheng Jin, Wentao Liu, Enze Xie, Wenhai Wang, Chen Qian, Wanli Ouyang, and Ping Luo. Differentiable hierarchical graph grouping for multi-person pose estimation. In *European Conference on Computer Vision*, pages 718–734. Springer, 2020. 2

[18] Sheng Jin, Lumin Xu, Jin Xu, Can Wang, Wentao Liu, Chen Qian, Wanli Ouyang, and Ping Luo. Whole-body human pose estimation in the wild. In *European Conference on Computer Vision*, pages 196–214. Springer, 2020. 1, 2, 4, 6, 7, 8

[19] Rawal Khirodkar, Timur Bagautdinov, Julieta Martinez, Su Zhaoen, Austin James, Peter Selednik, Stuart Anderson, and Shunsuke Saito. Sapiens: Foundation for human vision models. In *European Conference on Computer Vision*, pages 206–228. Springer, 2024. 1, 2

[20] Jungho Lee, Minhyeok Lee, Dogyoon Lee, and Sangyoun Lee. Hierarchically decomposed graph convolutional networks for skeleton-based action recognition. In *Proceedings of the IEEE/CVF International Conference on Computer Vision*, pages 10444–10453, 2023. 2, 5

[21] Jihyun Lee, Weipeng Xu, Alexander Richard, Shih-En Wei, Shunsuke Saito, Shaojie Bai, Te-Li Wang, Minhyuk Sung, Tae-Kyun Kim, and Jason Saragih. Rewind: Real-time egocentric whole-body motion diffusion with exemplar-based identity conditioning. In *Proceedings of the IEEE/CVF Conference on Computer Vision and Pattern Recognition*, pages 7095–7104, 2025. 2

[22] Han Li, Bowen Shi, Wenrui Dai, Yabo Chen, Botao Wang, Yu Sun, Min Guo, Chenlin Li, Junni Zou, and Hongkai

Xiong. Hierarchical graph networks for 3d human pose estimation. In *British Machine Vision Conference*, 2021. 2

[23] Jiefeng Li, Can Wang, Hao Zhu, Yihuan Mao, Hao-Shu Fang, and Cewu Lu. Crowdpose: Efficient crowded scenes pose estimation and a new benchmark. In *Proceedings of the IEEE/CVF Conference on Computer Vision and Pattern Recognition*, pages 10863–10872, 2019. 2, 6, 7

[24] Jiefeng Li, Siyuan Bian, Chao Xu, Zhicun Chen, Lixin Yang, and Cewu Lu. Hybrik-x: Hybrid analytical-neural inverse kinematics for whole-body mesh recovery. *IEEE Transactions on Pattern Analysis and Machine Intelligence*, 47(4): 2754–2769, 2025. 1

[25] Jing Lin, Ailing Zeng, Shunlin Lu, Yuanhao Cai, Ruimao Zhang, Haoqian Wang, and Lei Zhang. Motion-x: A large-scale 3d expressive whole-body human motion dataset. *Advances in Neural Information Processing Systems*, 36: 25268–25280, 2023. 1

[26] Jing Lin, Ailing Zeng, Haoqian Wang, Lei Zhang, and Yu Li. One-stage 3d whole-body mesh recovery with component aware transformer. In *Proceedings of the IEEE/CVF Conference on Computer Vision and Pattern Recognition*, pages 21159–21168, 2023. 1, 2, 6, 7

[27] Tsung-Yi Lin, Michael Maire, Serge Belongie, James Hays, Pietro Perona, Deva Ramanan, Piotr Dollár, and C Lawrence Zitnick. Microsoft coco: Common objects in context. In *European Conference on Computer Vision*, pages 740–755. Springer, 2014. 2, 5, 6, 7

[28] Xiao Lin, Yun Peng, Liuyi Wang, Xianyou Zhong, Minghao Zhu, Yi Feng, Jingwei Yang, Chengju Liu, and Qijun Chen. Cleanpose: Category-level object pose estimation via causal learning and knowledge distillation. In *Proceedings of the IEEE/CVF International Conference on Computer Vision*, pages 5990–6000, 2025. 2

[29] Yuejiang Liu, Riccardo Cadei, Jonas Schweizer, Sherwin Bahmani, and Alexandre Alahi. Towards robust and adaptive motion forecasting: A causal representation perspective. In *Proceedings of the IEEE/CVF Conference on Computer Vision and Pattern Recognition*, pages 17081–17092, 2022. 2

[30] Zhengxiong Luo, Zhicheng Wang, Yan Huang, Liang Wang, Tieniu Tan, and Erjin Zhou. Rethinking the heatmap regression for bottom-up human pose estimation. In *Proceedings of the IEEE/CVF Conference on Computer Vision and Pattern Recognition*, pages 13264–13273, 2021. 7

[31] Alejandro Newell, Zhiao Huang, and Jia Deng. Associative embedding: End-to-end learning for joint detection and grouping. *Advances in Neural Information Processing Systems*, 30, 2017. 6

[32] Yulei Niu, Kaihua Tang, Hanwang Zhang, Zhiwu Lu, Xian-Sheng Hua, and Ji-Rong Wen. Counterfactual vqa: A cause-effect look at language bias. In *Proceedings of the IEEE/CVF Conference on Computer Vision and Pattern Recognition*, pages 12700–12710, 2021. 2

[33] Judea Pearl. *Causality*. Cambridge university press, 2009. 2, 3

[34] Judea Pearl. Interpretation and identification of causal mediation. *Psychological methods*, 19(4):459, 2014. 2

[35] Judea Pearl, Madelyn Glymour, and Nicholas P Jewell. *Causal inference in statistics: A primer*. John Wiley & Sons, 2016. 2, 3, 1

[36] Wei Peng, Xiaopeng Hong, Haoyu Chen, and Guoying Zhao. Learning graph convolutional network for skeleton-based human action recognition by neural searching. In *Proceedings of the AAAI conference on artificial intelligence*, pages 2669–2676, 2020. 2

[37] Miroslav Purkrabek and Jiri Matas. Probpose: A probabilistic approach to 2d human pose estimation. In *Proceedings of the IEEE/CVF Conference on Computer Vision and Pattern Recognition*, pages 27124–27133, 2025. 2

[38] Jianning Quan and A Ben Hamza. Higher-order implicit fairing networks for 3d human pose estimation. *arXiv preprint arXiv:2111.00950*, 2021. 2

[39] Alessio Sampieri, Guido Maria D'Amely di Melendugno, Andrea Avogaro, Federico Cunico, Francesco Setti, Geri Skenderi, Marco Cristani, and Fabio Galasso. Pose forecasting in industrial human-robot collaboration. In *European Conference on Computer Vision*, pages 51–69. Springer, 2022. 1

[40] Lei Shi, Yifan Zhang, Jian Cheng, and Hanqing Lu. Skeleton-based action recognition with directed graph neural networks. In *Proceedings of the IEEE/CVF Conference on Computer Vision and Pattern Recognition*, pages 7912–7921, 2019. 2

[41] Yukun Su, Ruizhou Sun, Guosheng Lin, and Qingyao Wu. Context decoupling augmentation for weakly supervised semantic segmentation. In *Proceedings of the IEEE/CVF International Conference on Computer Vision*, pages 7004–7014, 2021. 2

[42] Ke Sun, Bin Xiao, Dong Liu, and Jingdong Wang. Deep high-resolution representation learning for human pose estimation. In *Proceedings of the IEEE/CVF Conference on Computer Vision and Pattern Recognition*, pages 5693–5703, 2019. 2, 6, 7

[43] Dongkai Wang, Shiliang Zhang, and Gang Hua. Robust pose estimation in crowded scenes with direct pose-level inference. *Advances in Neural Information Processing Systems*, 34:6278–6289, 2021. 2

[44] Jian Wang, Xiang Long, Yuan Gao, Errui Ding, and Shilei Wen. Graph-pcnn: Two stage human pose estimation with graph pose refinement. In *European Conference on Computer Vision*, pages 492–508. Springer, 2020. 2

[45] Shengze Wang, Jiefeng Li, Tianye Li, Ye Yuan, Henry Fuchs, Koki Nagano, Shalini De Mello, and Michael Stengel. Blade: Single-view body mesh estimation through accurate depth estimation. In *Proceedings of the IEEE/CVF Conference on Computer Vision and Pattern Recognition*, pages 21991–22000, 2025. 1

[46] Wenhai Wang, Enze Xie, Xiang Li, Deng-Ping Fan, Kaitao Song, Ding Liang, Tong Lu, Ping Luo, and Ling Shao. Pyramid vision transformer: A versatile backbone for dense prediction without convolutions. In *Proceedings of the IEEE/CVF International Conference on Computer Vision*, pages 568–578, 2021. 6

[47] Yue Wang, Yongbin Sun, Ziwei Liu, Sanjay E Sarma, Michael M Bronstein, and Justin M Solomon. Dynamic

graph cnn for learning on point clouds. *ACM Transactions on Graphics*, 38(5):1–12, 2019. 5, 3

[48] Jiahong Wu, He Zheng, Bo Zhao, Yixin Li, Baoming Yan, Rui Liang, Wenjia Wang, Shipei Zhou, Guosen Lin, Yanwei Fu, et al. Ai challenger: A large-scale dataset for going deeper in image understanding. *arXiv preprint arXiv:1711.06475*, 2017. 6

[49] Bin Xiao, Haiping Wu, and Yichen Wei. Simple baselines for human pose estimation and tracking. In *European Conference on Computer Vision*, pages 466–481, 2018. 6, 7

[50] Lumin Xu, Sheng Jin, Wentao Liu, Chen Qian, Wanli Ouyang, Ping Luo, and Xiaogang Wang. Zoomnas: Searching for whole-body human pose estimation in the wild. *IEEE Transactions on Pattern Analysis and Machine Intelligence*, 45(4):5296–5313, 2023. 2, 6

[51] Yufei Xu, Jing Zhang, Qiming Zhang, and Dacheng Tao. Vitpose: Simple vision transformer baselines for human pose estimation. *Advances in Neural Information Processing Systems*, 35:38571–38584, 2022. 2

[52] Yufei Xu, Jing Zhang, Qiming Zhang, and Dacheng Tao. Vitpose++: Vision transformer for generic body pose estimation. *IEEE Transactions on Pattern Analysis and Machine Intelligence*, 46(2):1212–1230, 2024. 1, 2, 6, 7

[53] Sen Yang, Zhibin Quan, Mu Nie, and Wankou Yang. Transpose: Keypoint localization via transformer. In *Proceedings of the IEEE/CVF International Conference on Computer Vision*, pages 11802–11812, 2021. 7

[54] Yiding Yang, Zhou Ren, Haoxiang Li, Chunluan Zhou, Xinchao Wang, and Gang Hua. Learning dynamics via graph neural networks for human pose estimation and tracking. In *Proceedings of the IEEE/CVF Conference on Computer Vision and Pattern Recognition*, pages 8074–8084, 2021. 2

[55] Zhendong Yang, Ailing Zeng, Chun Yuan, and Yu Li. Effective whole-body pose estimation with two-stages distillation. In *Proceedings of the IEEE/CVF International Conference on Computer Vision (ICCV) Workshops*, pages 4210–4220, 2023. 1, 2, 6, 7

[56] Hongwei Yi, Hualin Liang, Yifei Liu, Qiong Cao, Yandong Wen, Timo Bolkart, Dacheng Tao, and Michael J Black. Generating holistic 3d human motion from speech. In *Proceedings of the IEEE/CVF Conference on Computer Vision and Pattern Recognition*, pages 469–480, 2023. 1

[57] Bruce XB Yu, Zhi Zhang, Yongxu Liu, Sheng-hua Zhong, Yan Liu, and Chang Wen Chen. Gla-gcn: Global-local adaptive graph convolutional network for 3d human pose estimation from monocular video. In *Proceedings of the IEEE/CVF International Conference on Computer Vision*, pages 8818–8829, 2023. 2

[58] Yuhui Yuan, Rao Fu, Lang Huang, Weihong Lin, Chao Zhang, Xilin Chen, and Jingdong Wang. Hrformer: High-resolution vision transformer for dense predict. *Advances in Neural Information Processing Systems*, 34:7281–7293, 2021. 2, 7

[59] Luhui Yue, Junxia Li, and Qingshan Liu. Causal intervention learning for multi-person pose estimation. In *Asian Conference on Pattern Recognition*, pages 182–194. Springer, 2021. 2

[60] Ailing Zeng, Xiao Sun, Lei Yang, Nanxuan Zhao, Minhao Liu, and Qiang Xu. Learning skeletal graph neural networks for hard 3d pose estimation. In *Proceedings of the IEEE/CVF International Conference on Computer Vision*, pages 11436–11445, 2021. 2

[61] Dong Zhang, Hanwang Zhang, Jinhui Tang, Xian-Sheng Hua, and Qianru Sun. Causal intervention for weakly-supervised semantic segmentation. *Advances in Neural Information Processing Systems*, 33:655–666, 2020. 2

[62] Yi Zhang, Pengliang Ji, Angtian Wang, Jieru Mei, Adam Kortylewski, and Alan Yuille. 3d-aware neural body fitting for occlusion robust 3d human pose estimation. In *Proceedings of the IEEE/CVF International Conference on Computer Vision*, pages 9399–9410, 2023. 2

[63] Long Zhao, Xi Peng, Yu Tian, Mubbasir Kapadia, and Dimitris N Metaxas. Semantic graph convolutional networks for 3d human pose regression. In *Proceedings of the IEEE/CVF Conference on Computer Vision and Pattern Recognition*, pages 3425–3435, 2019. 2

[64] Hongwei Zheng, Han Li, Wenrui Dai, Ziyang Zheng, Chenglin Li, Junni Zou, and Hongkai Xiong. Hipart: Hierarchical pose autoregressive transformer for occluded 3d human pose estimation. In *Proceedings of the IEEE/CVF Conference on Computer Vision and Pattern Recognition*, pages 16807–16817, 2025. 2

CIGPose: Causal Intervention Graph Neural Network for Whole-Body Pose Estimation

Supplementary Material

A. Theoretical Foundation of Causal Intervention

This section provides the detailed theoretical support for the causal intervention framework introduced in the main paper Sec. 3. We first provide a formal derivation for the backdoor adjustment formula Eq. (1) using Pearl's *do*-calculus [35] and then offer a theoretical justification for our counterfactual replacement approximation Eq. (3).

Derivation of the Backdoor Adjustment Formula.

Our goal is to estimate the interventional distribution $P(Y|do(F))$, which represents the true causal effect of the keypoint embeddings F on the final prediction Y, isolated from the confounding influence of visual context C.

We recall the Structural Causal Model (SCM) from Fig. 2(a) of the main paper. This model defines the causal paths $C \to X \to F \to Y$ and the confounding paths $C \to X$ and $C \to Y$. The critical issue is the non-causal backdoor path $F \leftarrow X \leftarrow C \to Y$, which allows spurious correlations between F and Y based on the confounder C.

To block this path, we must adjust for the confounding variable C. Using the three rules of *do*-calculus [35], we can formally derive the backdoor adjustment formula presented in Eq. (1).

Given a causal graph $\mathcal{G}$, $\mathcal{G}_{\overline{X}}$ denotes the graph with incoming edges to X removed, and $\mathcal{G}_{\underline{X}}$ denotes the graph with outgoing edges from X removed.

- **Rule 1 (Insertion/deletion of observations):**

$$P(y|do(x), z, w) = P(y|do(x), w), \quad \text{if } (Y \perp Z|X, W)_{\mathcal{G}_{\overline{X}}}.$$

- **Rule 2 (Action/observation exchange):**

$$P(y|do(x), z, w) = P(y|x, z, w), \quad \text{if } (Y \perp X|Z, W)_{\mathcal{G}_{\underline{X}}}.$$

- **Rule 3 (Insertion/deletion of actions):**

$$P(y|do(x), do(z), w) = P(y|do(x), w), \quad \text{if } (Y \perp Z|X, W)_{\mathcal{G}_{\overline{X}, \overline{Z(W)}}}.$$

Our derivation proceeds as follows:

$$P(Y|do(F)) = \sum_c P(Y|do(F), c)P(c|do(F)) \tag{A1}$$

$$= \sum_c P(Y|do(F), c)P(c) \tag{A2}$$

$$= \sum_c P(Y|F, c)P(c) \tag{A3}$$

Step A1: We begin by applying the law of total probability, marginalizing over the confounder C.

Step A2: We apply **Rule 3** (Insertion/deletion of actions) to show $P(c|do(F)) = P(c)$. This holds if $(C \perp F|\emptyset)_{\mathcal{G}_{\overline{F}}}$. In the graph $\mathcal{G}_{\overline{F}}$, the edge $X \to F$ is removed. The only paths from C to F are $C \to X \quad F$ (d-separated) and $C \to Y \leftarrow F$. The latter is a v-structure and is blocked since Y is not a condition. Thus, C and F are d-separated, $(C \perp F|\emptyset)_{\mathcal{G}_{\overline{F}}}$ holds, and the intervention $do(F)$ has no effect on C.

Step A3: We apply **Rule 2** (Action/observation exchange) to show $P(Y|do(F), c) = P(Y|F, c)$. This holds if $(Y \perp F|C)_{\mathcal{G}_{\underline{F}}}$. In the graph $\mathcal{G}_{\underline{F}}$, the edge $F \to Y$ is removed. We must check if any other paths connect F and Y, given C. The only other path is the backdoor path $F \leftarrow X \leftarrow C \to Y$. Since we are conditioning on C, this path is blocked at C. Therefore, $(Y \perp F|C)_{\mathcal{G}_{\underline{F}}}$ holds, and we can replace the action $do(F)$ with the observation F.

This completes the formal derivation of Eq. (1) in the main paper.

Justification for Counterfactual Replacement.

As stated in the main text, Eq. (A3) (the backdoor adjustment formula) is intractable to compute because C is unobserved, high-dimensional, and impossible to sum over. Our Causal Intervention Module (CIM) approximates this intervention by performing a *counterfactual replacement*, $do(f_k := z_k)$, as defined in Eq. (3).

The theoretical justification is as follows:

1. **Goal:** The target distribution $P(Y|do(F)) = \mathbb{E}_c[P(Y|F, c)]$ represents the causal effect of F on Y, averaged over all possible contexts c. This conceptually creates a context-invariant, unbiased representation.
2. **Problem:** The observed embedding $f_k \in F$ is confounded. It is a descendant of C via the path $C \to X \to F$. This dependency on C is precisely what opens the spurious backdoor path $F \leftarrow X \leftarrow C \to Y$.
3. **Our Approximation:** We introduce a learnable canonical embedding table $Z \in \mathbb{R}^{K \times d_{emb}}$. As a shared global parameter matrix, Z is reused across all images and is not conditioned on the current instance. Hence, it is optimized end-to-end while remaining independent of any specific input image X_i and its associated confounder C_i; that is, $Z \perp C$ by construction.
4. **The Intervention:** When our CIM identifies a confounded embedding f_k (via $s_c(k)$) and replaces it with its corresponding canonical ideal $z_k \in Z$, it is performing the counterfactual operation $do(f_k := z_k)$. This op-

eration replaces a variable that is dependent on C (the original f_k) with a variable that is independent of C (the canonical z_k).

5. **The Effect:** This replacement physically severs the causal link $C \rightarrow X \rightarrow F$ at the feature level. For the intervened embedding $f'_k = z_k$, the backdoor path $F' \leftarrow X \leftarrow C \rightarrow Y$ is broken because f'_k is no longer a descendant of C or X.

The shared/global parameterization of Z is central to this approximation. Each row z_k accumulates updates from many images whenever keypoint type k is selected for intervention, so sample-specific contextual cues are not tied to any single replacement vector. Instead, optimization reinforces what is consistently useful for predicting the same anatomical keypoint across diverse contexts, which is precisely the intended context-invariant prior. By computing $P(Y|F')$ where F' is the deconfounded set, we force the model to reason using the context-invariant ideal z_k instead of the confounded evidence f_k. This serves as a practical, sample-specific approximation of the full, intractable summation over all contexts $\sum_c$. The counterfactual consistency loss defined in Eq. (6) further ensures that this replacement is targeted, regularizing Z to be a meaningful "ideal" representation for stable keypoints.

B. Further Analysis of Predictive Uncertainty

As discussed in the main paper Sec. 1 and Sec. 3, our framework posits that predictive uncertainty is an effective proxy for identifying confounded keypoint representations. Confounders like heavy occlusion create a conflict between the model's spuriously learned priors from $C \rightarrow Y$ and the visual evidence from $F \rightarrow Y$, resulting in high epistemic uncertainty.

Beyond-occlusion quantitative evidence. The occlusion-based analysis in Fig. 3 validates $s_c(k)$ against a clearly defined confounder. To test whether the proxy also captures broader keypoint difficulty beyond explicit occlusion labels, we perform a within-instance top-n enrichment analysis on the COCO-WholeBody validation set. For instance i, let V_i be the set of visible keypoints and let $T_i = \mathrm{TopK}(\{s_{c,i}(k)\}, n)$ be the keypoints selected by the proxy. We define

$$\Delta_i = \frac{1}{|T_i|} \sum_{k \in T_i} e_i(k) - \frac{1}{|V_i \setminus T_i|} \sum_{k \in V_i \setminus T_i} e_i(k), \qquad (7)$$
$$e_i(k) = \|\hat{\mathbf{p}}_i(k) - \mathbf{p}_i(k)\|_2 ,$$

where $e_i(k)$ is the localization error of keypoint k. A positive Δ_i means that, within the same instance, the keypoints selected by s_c incur larger error than the remaining visible keypoints.

As shown in Tab. 5, the enrichment is strongly positive and widens on progressively harder subsets. This indicates that s_c systematically concentrates on intrinsically harder keypoints within an instance, including cases driven by clutter, blur, and truncation rather than only binary occlusion status.

Table 5. Within instance top-n enrichment on COCO-WholeBody. Keypoints selected by s_c exhibit larger localization error than the remaining keypoints in the same instance. Easy-drop p denotes the fraction of easiest instances removed when forming harder subsets, and 95% CIs are percentile bootstrap intervals over instances.

Easy-drop p	Kept inst.	Mean $\bar{\Delta}$ (px)	95% CI
0.00	104,125	8.47	[8.20, 8.72]
0.30	72,888	10.14	[9.78, 10.48]
0.50	52,063	10.45	[10.02, 10.87]

Qualitative example. In Fig. 3 of the main text, we quantitatively validated the proxy with occlusion labels. Here, in Fig. 7, we provide the qualitative example referenced in the main text.

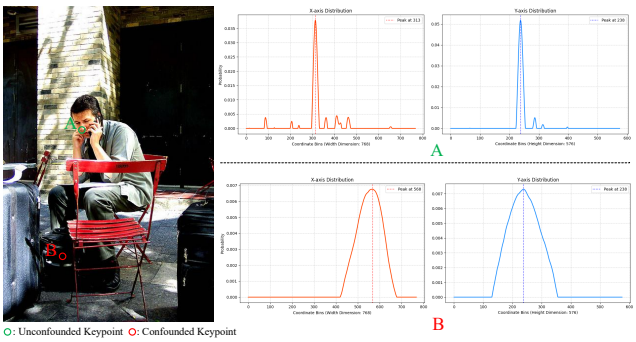

Figure 7. Visualization of posterior probability distributions. (A) For an unconfounded keypoint (green circle, nose), the distributions exhibit sharp, high peaks, indicating low uncertainty. (B) For a confounded keypoint (red circle, left ankle), which is occluded and in shadow, the distributions are diffuse with low peaks, signaling high predictive ambiguity.

This example visually demonstrates the mechanism of CIGPose:

1. **Confounder Identification:** The occluded L-Ankle leads to high predictive uncertainty, producing a diffuse posterior distribution.
2. **Causal Intervention:** Our model computes a high $s_c(k)$ for this keypoint, triggering the counterfactual replacement $do(f_{L\text{-}Ankle} := z_{L\text{-}Ankle})$.
3. **Deconfounded Reasoning:** The Hierarchical GNN, now operating on the "clean" embedding set F', leverages anatomical constraints from visible keypoints (such as the L-Knee) to infer the position of the occluded joint, resulting in an anatomically plausible prediction.

C. Expanded Implementation Details

This section provides additional details on network architecture and training settings, supplementing Sec. 3 and Sec. 4.2 of the main paper.

Network Architecture Details. Our CIGPose framework builds upon the RTMPose [15] architecture, introducing a novel prediction head. Below, we detail the components of this head.

- **Backbone and Feature Processing**: We employ a CSPNeXt backbone as our keypoint encoder. For an input image of size $H \times W$, the backbone outputs a feature map of size $\frac{H}{32} \times \frac{W}{32}$ with 1280 channels. This feature map is then processed by a Gated Attention Unit (GAU) with hidden dimensions of 512, which extracts the initial keypoint embeddings $F \in \mathbb{R}^{B\times K\times 512}$, where B is the batch size and K is the number of keypoints ($K = 133$ for the COCO-WholeBody dataset, and $K = 17$ for the COCO and CrowdPose datasets).
- **Causal Intervention Module (CIM)**: The CIM takes the initial embeddings F as input. First, two separate linear layers project F to generate initial 1D SimCC predictions $(P_{k,x}, P_{k,y})$. These are used to calculate the confounder score $s_c(k)$ for each keypoint per Eq. (2). The module then identifies the top-n most confounded embeddings and replaces them with corresponding vectors from a shared canonical embedding table $Z \in \mathbb{R}^{K\times 512}$. This table is implemented as a standard `Embedding` layer, initialized with a normal distribution $\mathcal{N}(0, 0.01^2)$ and optimized end-to-end.
- **Hierarchical GNN**: The deconfounded embeddings F' are processed by a hierarchical GNN to model anatomical constraints, as discussed in Sec. 3.3.
  - *Intra-Part Modeling*: The first stage uses an `EdgeConv` [47] layer that operates over the standard anatomical skeleton graph $\mathcal{G}_p$. This layer models local kinematics by computing edge features (the difference between connected node features concatenated with the source node feature) and aggregating them via a shared MLP, which is implemented using a 1×1 2D convolution.
  - *Inter-Part Attention*: The second stage uses an `AttentionModule` to capture long-range dependencies. It first computes an aggregate representation for each predefined semantic keypoint group by averaging the features of its constituent keypoints. These group-level features are then refined by passing them through a second `EdgeConv` layer defined over a fully-connected graph of all groups. The output is then used to generate channel-wise attention weights via a linear layer and a sigmoid function, per Eq. (4). These weights modulate the keypoint features, enabling the model to reason about global inter-part relationships.

  The full skeleton graph definition and the list of semantic groups are specified in the model configuration files.

Joint optimization of the canonical embedding table. For a mini-batch of size B, the counterfactual replacement in Eq. (3) is applied instance-wise as

$$\begin{aligned} f'_{b,k} &= (1 - m_{b,k}) f_{b,k} + m_{b,k} z_k, \\ m_{b,k} &= \mathbf{1}[k \in \mathcal{I}_b], \end{aligned} \tag{8}$$

where $\mathcal{I}_b = \mathrm{TopK}(\{s_c(b,k)\}_{k=1}^{K}, n)$ is the selected set for instance b, and the mask $M = \{m_{b,k}\}$ is broadcast along the embedding dimension. Let $H_\theta(\cdot)$ denote the prediction head following the encoder and hierarchical graph reasoning. The counterfactual path computes $P_{\text{cf}}(Y) = H_\theta(F')$, while the observational prediction $P_{\text{obs}}(Y) = H_\theta(F)$ is used only through the stop-gradient target in Eq. (6). Therefore, gradients flow into the selected rows of Z according to

$$\frac{\partial \mathcal{L}}{\partial z_k} = \sum_{b=1}^{B} m_{b,k} \frac{\partial \mathcal{L}}{\partial f'_{b,k}}, \tag{9}$$

while rows that are not selected in the current mini-batch receive zero gradient from that step. Thus, Z is optimized jointly with the network parameters θ under $\mathcal{L} = \mathcal{L}_{\text{kpt}} + \lambda \mathcal{L}_{\text{cf}}$.

The corresponding training procedure is summarized in Algorithm 1.

Algorithm 1: Training: joint update of (θ, Z)

Input: mini-batch images X; GT distributions $\{Q_{b,k}\}$; budget n; weight λ
Output: updated parameters (θ, Z)
$F \leftarrow E_\theta(X)$ `// keypoint embeddings`
Compute $(P_{b,k,x}, P_{b,k,y})$ and scores $s_c(b,k)$ (Eq. (2))
for $b = 1$ **to** B **do**
  $\mathcal{I}_b \leftarrow \mathrm{TopK}(\{s_c(b,k)\}_{k=1}^{K}, n)$
  $m_{b,k} \leftarrow \mathbf{1}[k \in \mathcal{I}_b], \forall k \in \{1, \ldots, K\}$
$F' \leftarrow (1 - M) \odot F + M \odot Z$ `// Eq. (3),` $M = \{m_{b,k}\}$
$P_{\text{cf}} \leftarrow H_\theta(F')$
$\tilde{P}_{\text{obs}} \leftarrow \mathrm{sg}[H_\theta(F)]$ `// stop-grad target`
$\mathcal{L}_{\text{kpt}} \leftarrow \sum_{b,k} w_{b,k} D_{\text{KL}}(Q_{b,k} \,\|\, P_{\text{cf}}(Y_{b,k}))$
$\mathcal{L}_{\text{cf}} \leftarrow \frac{1}{\sum_b |S_b|} \sum_b \sum_{k\in S_b} D_{\text{KL}}(\tilde{P}_{\text{obs}}(Y_{b,k}) \,\|\, P_{\text{cf}}(Y_{b,k}))$
`//` S_b`: stable (non-intervened) set`
$\mathcal{L} \leftarrow \mathcal{L}_{\text{kpt}} + \lambda \mathcal{L}_{\text{cf}}$; update (θ, Z) by AdamW

Training settings. Our training settings largely follow that of RTMPose [15], including a two-stage fine-tuning approach. The key hyperparameters for our main experiments (CIGPose-x on COCO-WholeBody) are summarized in Tab. 6.

Table 6. Key training hyperparameters for the CIGPose-x model.

Hyperparameter	Value
Optimizer	AdamW
Base Learning Rate	2×10^{-3}
Weight Decay	0.05
LR Schedule	Cosine Annealing
Warm-up Iterations	1000
Max Gradient Norm	35
Training Epochs	420
Stage-2 Epochs	150
λ for $\mathcal{L}_{cf}$	0.1 (Ablated in Sec. E)
Train Batch Size	32 (per GPU)
Intervention n	13 (Ablated in Sec. E)

D. Data Augmentation

We adopt a two-stage data augmentation strategy to enhance model robustness, corresponding to the two-stage training detailed in Sec. C.

- **Stage 1 (Epoch 1-270)**: This stage uses aggressive augmentation. It includes random horizontal flipping, random half-body transforms, random bounding box transformations (scaling from 0.5x to 1.5x, rotation of $\pm 90°$), top-down affine transforms, and YOLOX-style HSV color jittering. To simulate heavy occlusions, we also apply Albumentation transforms including `Blur` (p=0.1), `MedianBlur` (p=0.1), and `CoarseDropout` (p=1.0, max_holes=1, max_height=128, max_width=128).
- **Stage 2 (Epoch 271-420)**: For the final fine-tuning stage, the augmentation intensity is reduced to allow the model to converge on cleaner data. Specifically, the random bounding box transform is modified to perform only scaling and rotation (shift factor is set to 0), and the probability of applying `CoarseDropout` is lowered to 0.5.

E. Additional Experimental Analysis

We conduct further experiments on the COCO-WholeBody [18] validation set to analyze key components of our framework, supplementing the main ablations in Sec. 4.4. Unless otherwise specified, these studies use the CIGPose-l (384×288) model.

Analysis of Intervention Frequency. To verify that our Causal Intervention Module effectively targets keypoints susceptible to confounding, we analyze the intervention frequency for different body parts on the COCO-WholeBody validation set. As shown in Tab. 7, the intervention rates are highest for feet, hands, and legs. These are the body parts most frequently affected by common visual confounders such as occlusion, motion blur, and truncation. This empirical result provides evidence that our uncertainty-based proxy successfully identifies and targets the most confounded keypoints.

Table 7. Intervention frequency per body part on COCO-WholeBody. The module intervenes most often on extremities, which are most prone to confounding.

Body Part	Intervention Freq. (%)
Face	0.67
Torso	0.16
Arms	0.24
Hands	0.90
Legs	0.89
Feet	1.36

Sensitivity to Consistency Loss Weight λ. The counterfactual consistency loss, $\mathcal{L}_{cf}$ which is defined in Eq. (6), is critical for ensuring that interventions are meaningful and that the canonical embeddings Z are learned effectively. We analyze the model's performance while varying the loss weight λ.

Table 8. Effect of the counterfactual consistency loss weight λ.

λ	Whole-Body AP (%)
0	65.8
0.01	66.1
0.1	**66.3**
0.5	65.9

As shown in Tab. 8, removing the consistency loss entirely ($\lambda = 0$) leads to a 0.5 AP drop. This demonstrates that without this regularization, the model struggles to learn stable and meaningful canonical embeddings. A larger weight ($\lambda = 0.5$) also slightly degrades performance, likely by overly constraining the GNN and preventing it from fully leveraging the deconfounded features. Our chosen value of $\lambda = 0.1$ provides the best trade-off.

Analysis of Intervention Strategy and Parameter n. All main experiments use a fixed 'top-n' intervention strategy during training. For comparison, we also evaluate a threshold-based strategy. Formally, given a predefined threshold τ, the threshold strategy defines the set of keypoints selected for intervention, $\mathcal{K}_{\text{conf}}$, as:

$$\mathcal{K}_{\text{conf}} = \{k \mid s_c(k) > \tau\}$$

where $s_c(k)$ is the confounder score defined in Eq. (2). This means we intervene on any keypoint whose uncertainty-based score surpasses the threshold.

The results in Tab. 9 show that the 'top-n' strategy is more effective. We hypothesize that this is because it pro-

Table 9. Comparison of intervention strategies during training. The fixed-budget 'top-n' strategy provides a more stable and effective training signal, with $n = 13$ yielding the best result on COCO-WholeBody.

Intervention Strategy (Training)	**Whole-Body AP (%)**
Threshold $\tau = 0.7$	65.9
Threshold $\tau = 0.8$	65.8
Top-n ($n = 11$)	66.1
Top-n ($n = 13$)	**66.3**
Top-n ($n = 15$)	66.0

vides a more stable training signal by ensuring a fixed number of keypoints n are intervened upon in each iteration. The 'threshold' approach can be noisy, as the number of interventions can vary dramatically between samples, potentially making it more difficult for the model to learn effective canonical embeddings. We also ablate the value of n (for training) and find $n = 13$ (10% of $K = 133$ keypoints) to be optimal.

F. Limitations

Limitations of Causal Intervention via Replacement. The Causal Intervention Module (CIM) approximates the intractable do-operation by identifying confounded embeddings f_k, as signaled by high uncertainty $s_c(k)$, and replacing them with context-invariant canonical embeddings z_k. While effective for occlusion, this $do(f_k := z_k)$ substitution carries a risk of over regularization. The core assumption is that high uncertainty correlates with visual confounding. However, this assumption can be violated in cases of valid but statistically rare poses, such as the intimate head-to-head interaction shown in Fig. 8 (top). In such scenarios, the visual evidence f_k is anatomically correct but lies on the tail of the pose distribution. The model exhibits high epistemic uncertainty simply due to the sample's out-of-distribution nature. Consequently, CIM may incorrectly flag these valid embeddings as confounded and replace them with z_k, which represents a mean or canonical ideal. This can regularize the prediction too aggressively, discarding correct fine-grained geometry in favor of a generic high-likelihood pose.

Limitations of Uncertainty as a Confounding Proxy. The second limitation relates to the proxy $s_c(k)$ itself. Our quantitative validation in Fig. 3 and Tab. 5 shows that $s_c(k)$ is effective at identifying ambiguity-induced difficulty, including occlusion and harder non-occlusion cases. However, it fails when the model falls victim to confident semantic errors. As illustrated in Fig. 8 (bottom), the model hallucinates a human skeleton on a street lamp. This error stems from spurious correlations learned during training—specifically, associating vertical linear structures with limbs. Critically, the model does not view this as an ambiguous state; it predicts the false positive with high confidence (low uncertainty), likely due to the strong shape similarity fulfilling the top-down detector's prior. Because $s_c(k)$ remains low, the CIM mechanism is bypassed entirely. This highlights a fundamental boundary of our framework: it is adept at rectifying uncertain representations but lacks an inherent rejection mechanism for confident misidentification caused by strong contextual confusion.

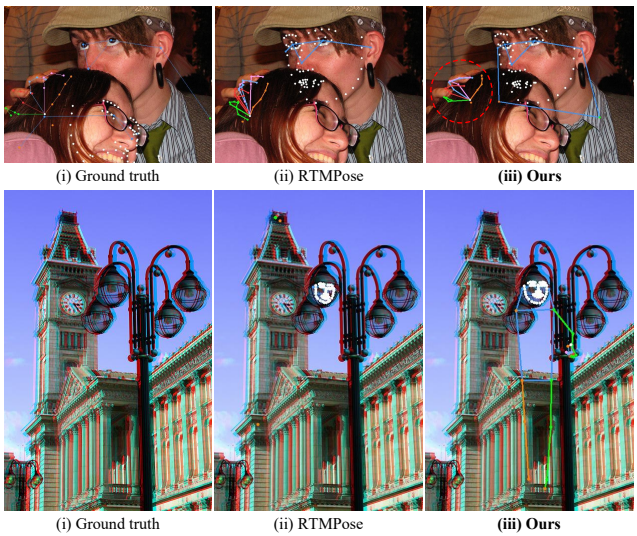

Figure 8. Visualization of failure cases.

G. More Qualitative Results

Figure 9. Qualitative comparison of CIGPose-x against the baseline RTMPose-x [15] on challenging images. From left to right: input image, RTMPose-x, and CIGPose-x.